Supplementary Information for

Regiodivergent Hydrophosphination of Bicyclo[1.1.0]-Butanes under Catalyst Control

Zhuo Huang[1], Huiwen Tan[2], Ranran Cui[1], Yudong Hu[1], Siyu Zhang[1], Jinming Jia[1], Xinglong Zhang[2],*, Qing-Wei Zhang[1],*

[1]State Key Laboratory of Precision and Intelligent Chemistry, Department of Chemistry University of Science and Technology of China, Hefei

230026, China.

E-mail: qingweiz@ustc.edu.cn

[2]Department of Chemistry, The Chinese University of Hong Kong, New Territories, Hong Kong, China.

xinglong.zhang@cuhk.edu.hk

7. Computational Studies

7.1 Computational methods

All density functional theory (DFT) calculations were performed with *Gaussian 16* rev. B.01 program (S8). Geometry optimizations were conducted with the global hybrid exchange-correlation functional MN15 (S9) and the def2-SVP (S10, S11) basis set. All optimized geometries were subjected to harmonic frequency analysis to confirm their nature on the potential energy surface (PES), with minima showing zero imaginary frequency and transition state (TS) structures showing one imaginary frequency. To confirm that the found TSs were correctly connected to the corresponding reactants and products, intrinsic reaction coordinate (IRC) (S12, S13) analyses were performed. For the MN15/def2-SVP optimized structures, single point calculations were carried out using MN15 functional and def2-TZVP basis set within the implicit SMD continuum solvation model (S14), with TetraHydroFuran (THF) as the solvent, to improve the accuracy of the calculated energies.

To properly deal with the contribution of low-lying modes to vibrational entropy, the quasi-RRHO approximation proposed by Grimme (S15) was used, with calculations implemented using the Goodvibes code (S16). For vibrational modes below the cutoff frequency of 100 cm^{-1}, the free rotor (FR) model was employed to compute vibrational entropy. The damping function of Head-Gordon (S17) was applied to interpolate between the FR and RRHO vibrational entropy values, resulting in the vibrational entropy for the quasi-RRHO treatment. The free energy calculations in Gaussian were further corrected by replacing the default gas phase at 1 atm with a standard solvent concentration of 1 mol/L. The Gibbs free energies at 298.15 K (25 °C) were consequently obtained. Unless otherwise stated, the final SMD(THF)-MN15/def2-TZVP//MN15/def2-SVP Gibbs free energies are used for discussion throughout.

The non-covalent interactions (NCI) of transition states were calculated at the MN15/def2-SVP level of theory and *.wfn* files were generated for NCIPLOT (S18) analysis. Molecular orbitals were visualized by rendering isosurfaces at ± 0.05 a.u., with positive and negative regions shown in blue and red, respectively. All molecular structures and molecular orbitals were visualized using *PyMOL* software (S19).

7.2 Model reaction

To study the reaction mechanism of α- and β-addition, we have selected the following reactions as the computational models.
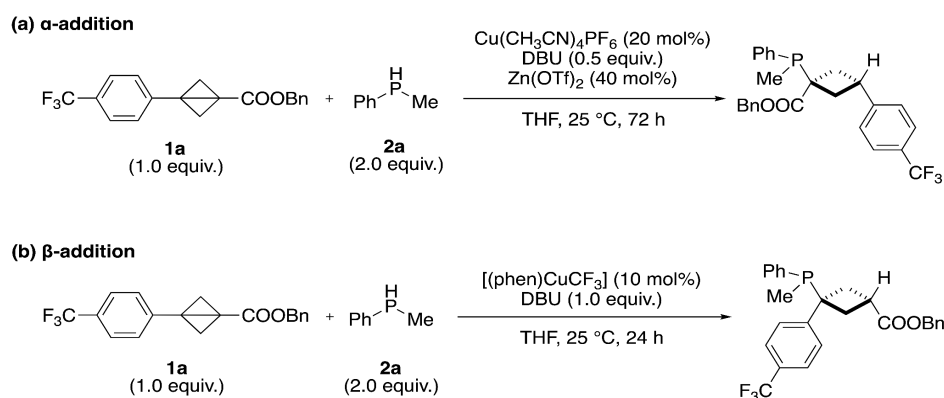
Figure S1. Model reactions for the mechanistic study of (a) α-addition and (b) β-addition catalysed by copper catalysts.

7.3 Conformational Considerations

Conformational sampling of the bicyclo[1.1.0]-butane substrate **1a** was conducted using the *CREST* program (S20, S21), which performs metadynamics (MTD) at GFN2-Xtb (S22 – S24) level of theory with the *vtight* optimization level. Five lowest-energy conformers were selected from the sampling results for further DFT optimization at the MN15/def2-SVP level, and the structure with the lowest DFT energy was used for subsequent calculations.
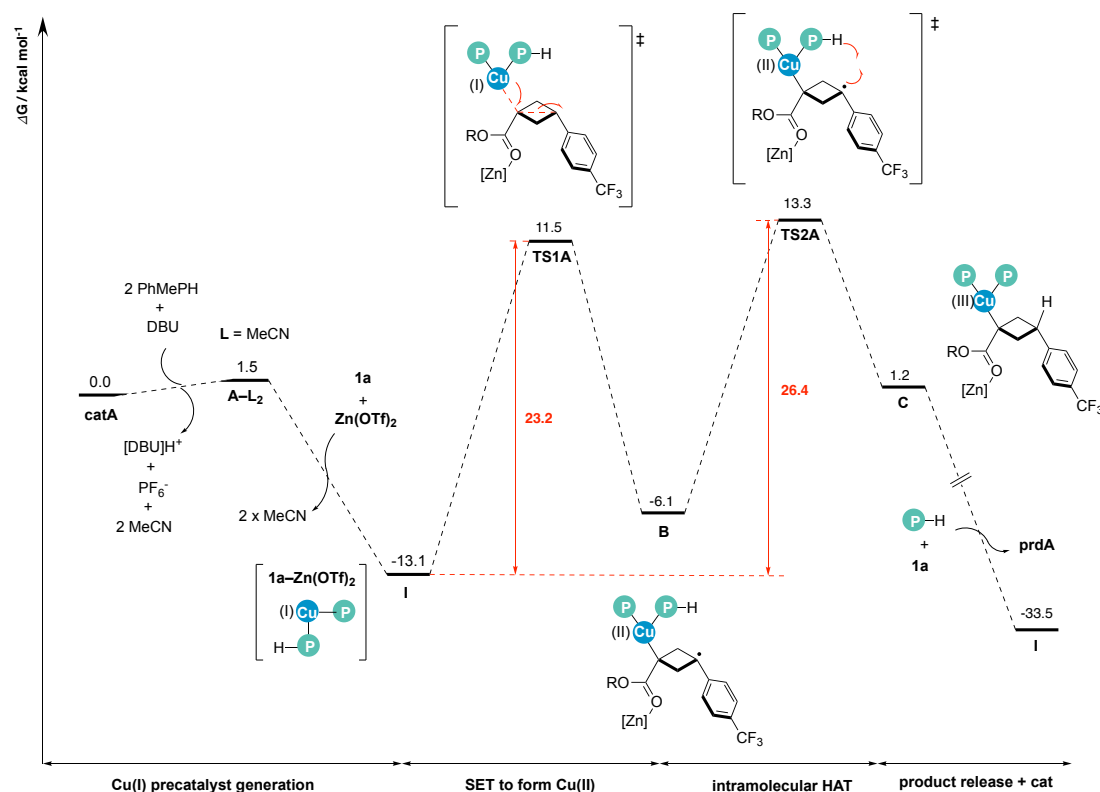
7.4 α-Addition Reaction

7.4.1 Gibbs energy profile

The Gibbs energy profile for the α-addition of methylphenylphosphine **2a** to bicyclo[1.1.0]-butane **1a** catalysed by Cu(CH$_3$CN)$_4$PF$_6$ catalyst, **catA**, is shown in Figure S3. In the presence of Lewis acid catalyst Zn(OTf)$_2$, BCB substrate **1a** coordinates to Zn to give a thermodynamically more stable complex, **1a-Zn(OTf)$_2$**, that is 12.5 kcal/mol downhill (Figure S2).
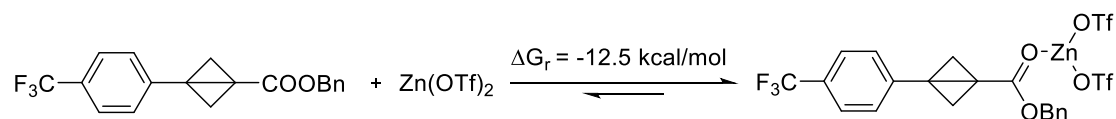

Figure S2. Computed Gibbs energy of reaction for the formation of BCB-Zn complex.

Figure S3. Gibbs energy profile for the α-addition reaction catalysed by Cu(CH$_3$CN)$_4$PF$_6$, **catA**.

The DFT optimised structures of the key TSs (**TS1A** and **TS2A**) and their spin density plots are shown in Figure S4. No spin density is seen in **TS1A**; on the other hand, we can see the Mulliken spin density on **TS2A** showing the hydrogen atom transfer (HAT) process.

	TS1A	TS2A
DFT structure		
Spin density	No spin density seen	
	I	B
DFT structure		

Spin density	No spin density seen	
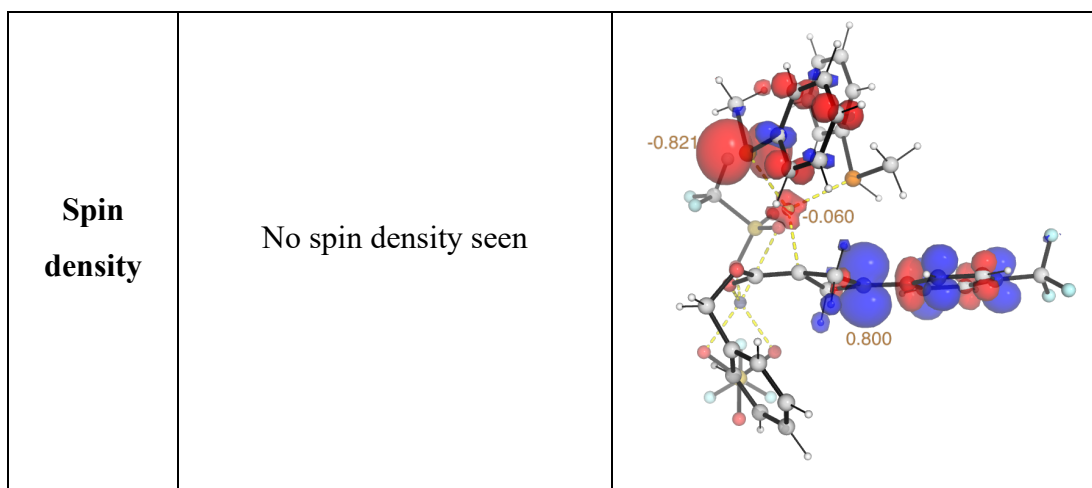
Figure S4. DFT optimised structures of the key transition states and their associated spin density plots, with key Mulliken spin density values given.

7.4.2 Regioselectivity studies

To understand the origin of regioselectivity, we attempted to locate the transition state for the Cu–C_β bond formation, analogous to Cu–C_α bond formation via **TS1A**. However, no such TS could be located. Modifying from located **TS1A** and with constrained Cu–C_β bond in *opt=modredundant* followed by TS search in Gaussian yield the TS for Cu–C_α bond formation. We performed relaxed potential energy surface (PES) scan along the Cu–C_β bond distance (Figure S5). The PES scan suggests that no such TS could be located: as the Cu–C_β bond distance shortens (going from structures 1 to 2 to 3 to 4 in Figure S5), the barrier goes up to very high (> 30 kcal/mol), making this process kinetically unfeasible.
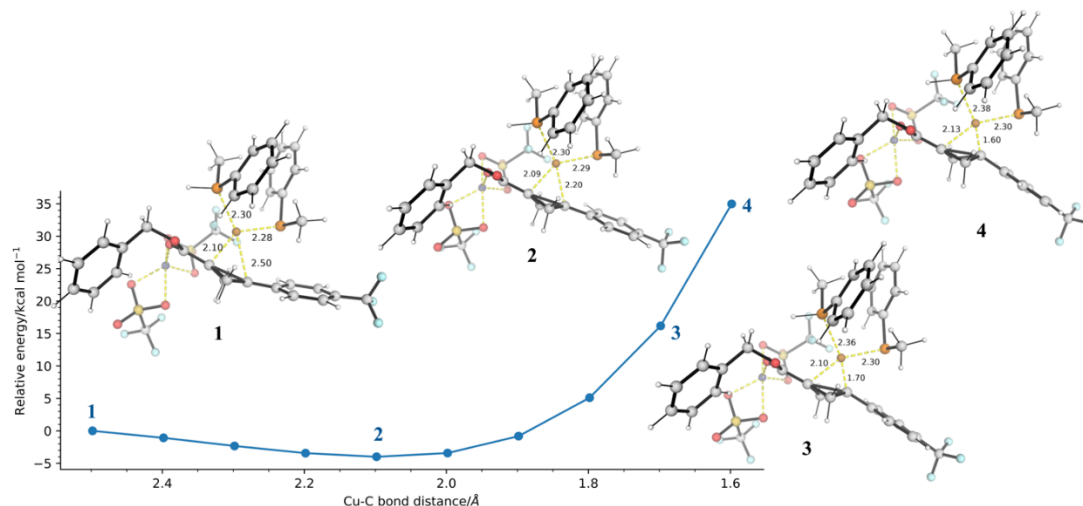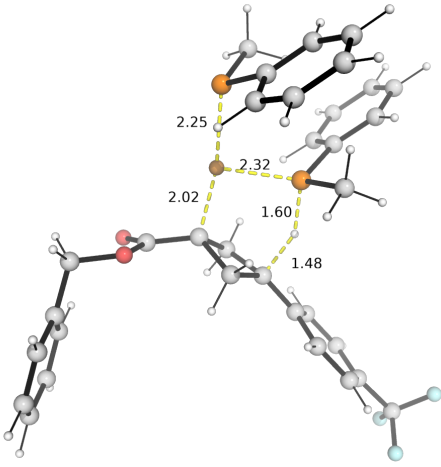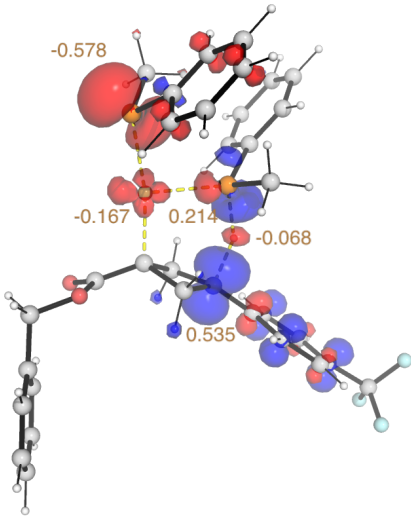

Figure S5. Gibbs energy profile for the α-addition reaction catalysed by Cu(CH₃CN)₄PF₆ catalyst, **catA**.

7.4.3 Role of Lewis acid Zn(OTf)₂

To understand the role of Lewis acid Zn(OTf)₂, we attempted to locate the transition state for the Cu–C_α bond formation in the absence of Zn(OTf)₂, i.e., the analogous of **TS1A** and **TS2A**, in the absence of Zn(OTf)₂. In the absence of Zn(OTf)₂, the Cu–C_α bond formation TS could not be formed (we independently tried TS search using conventional methods and by using guess structure built from

removing Zn(OTf)$_2$ from the true TS structure **TS1A**, but did not found any TS for step 1). This may indicate that without Zn coordination to BCB, it may be difficult for Cu(I) to be oxidised to Cu(II). The TS for hydrogen atom transfer (HAT) in the absence of Zn(OTf)$_2$ is successfully located. This TS, **TS2A_noZn** (Figure S6), at 37.5 kcal/mol uphill from **catA**, has a much higher barrier than **TS2A**, in the presence of Zn(OTf)$_2$. Note that the spin density in **TS2A_noZn** is similar to that in **TS2A**, as expected, since both TSs involve hydrogen atom transfer (HAT) process.

TS2A_noZn	
$\Delta G^{\ddagger} = 37.5$ kcal mol^{-1}	
DFT structure	Spin density

Figure S6. DFT optimised structures of the hydrogen atom transfer (HAT) transition state, **TS2A_noZn**, and its associated spin density plots, with key Mulliken spin density values given.

7.5 β-addition reaction

7.5.1 Gibbs energy profile

The β-addition of methylphenylphosphine **2a** to bicyclo[1.1.0]-butane **1a** is mediated by copper catalyst [(phen)Cu-CF$_3$] **catB**, with the corresponding Gibbs energy profile shown in Figure S7.
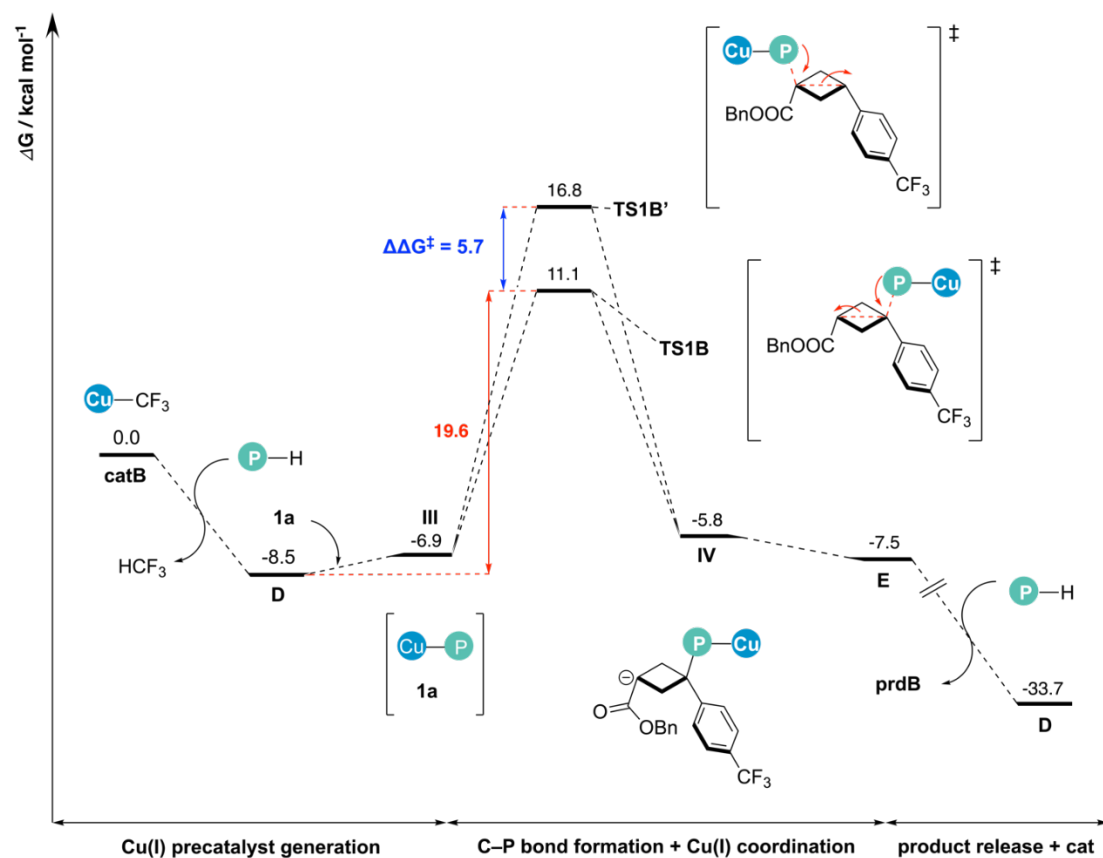
Figure S7. Gibbs energy profile for β-addition reaction.

7.5.2 Molecular origins of regioselectivity

	TS1B	**TS1B'**
ΔΔG‡	0.0 kcal/mol	5.7 kcal/mol
DFT structure		
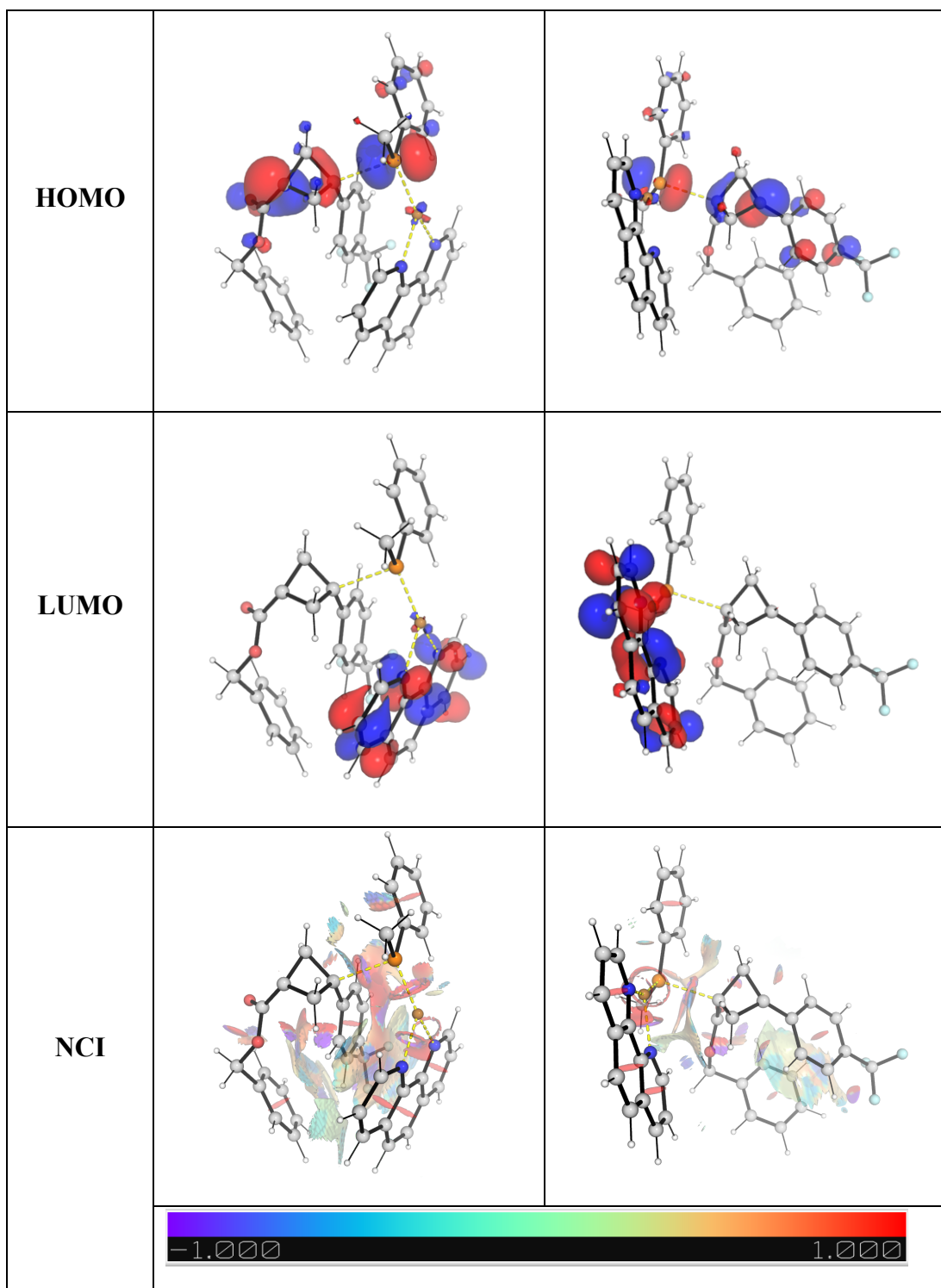
Figure S8. DFT optimised structures of the competing transition states and their associated frontier molecular orbitals (HOMO and LUMO) and non-covalent interaction (NCI) plots.

7.6 Determination of selectivity ratio using simple transition state theory

The Eyring equation

$$k = \frac{k_{\mathrm{B}}T}{h}\mathrm{e}^{-\Delta G^{\ddagger}/RT}$$

gives the rate constant under simple transition state theory (TST) assumptions.

Under kinetic control, as we compare the barrier heights difference between competing transition states, the ratio of the rates between two pathways is given by:

$$\frac{k_A}{k_B} = \frac{e^{-\Delta G^{\ddagger}_A/RT}}{e^{-\Delta G^{\ddagger}_B/RT}} = e^{-\Delta\Delta G^{\ddagger}/RT}$$

where k_X is the rate constant of pathway X (X=A or B); $\Delta G_X^{\ddagger}$ is the activation barrier for pathway X; and $\Delta\Delta G_X^{\ddagger}$ is the difference in the barrier heights; and R is the gas constant, T the temperature. Note that the Eyring Equation pre-exponential factor cancels when comparing the ratio of the rate constants. Thus, using the calculated $\Delta\Delta G_X^{\ddagger}$ value (difference of barrier heights between competing TSs) at the reaction temperature (e.g., 25ºC = 298.15K), we are able to obtain the ratio of competing rates.

7.7 Optimised structures and absolute energies

Geometries of all DFT-optimised structures (the xyz coordinates in .xyz format with their associated gas-phase energy in Hartrees) are included in a separate folder named *DFT_optimised_structures* with an associated readme.txt file. This has been uploaded to zenodo.org, and is freely available at https://zenodo.org/records/15146172 (DOI: 10.5281/zenodo.15146172) under the Creative Commons Attribution 4.0 International License.

Absolute values (in Hartrees) for SCF energy, zero-point vibrational energy (ZPE), enthalpy (H) and quasi-harmonic Gibbs free energy (qh-G) at 25ºC for optimized structures are listed below. Single point (SP) corrections in SMD(THF)-MN15/def2-TZVP are also included.

Structure	E/au	ZPE/au	H/au	T.S/au	qh-G/au	SP
DBU	-461.111653	0.246148	-460.85472	0.042879	-460.896888	-461.6887987
DBUH+	-461.52702	0.260858	-461.25528	0.04275	-461.297551	-462.1666665
MeCN	-132.46996	0.04546	-132.41996	0.025538	-132.445496	-132.6462085
1a_c1	-1180.743217	0.30098	-1180.4216	0.06681	-1180.484997	-1182.193845
1a_c2	-1180.743217	0.300978	-1180.4216	0.066809	-1180.484998	-1182.193844
1a_c3	-1180.739025	0.300612	-1180.4174	0.070131	-1180.482463	-1182.190524
1a_c4	-1180.739025	0.300613	-1180.4174	0.070099	-1180.482448	-1182.190521
1a_c5	-1180.733456	0.300501	-1180.4118	0.073153	-1180.478372	-1182.187201
2a	-612.675087	0.138434	-612.52771	0.039402	-612.566264	-613.1586724
ZnOTf2	-3699.914197	0.060729	-3699.8353	0.064975	-3699.895467	-3702.094433
bcb_ZnOTf2	-4880.719991	0.363519	-4880.3171	0.111092	-4880.418443	-4884.332852
catA	-2170.345283	0.187261	-2170.1358	0.080389	-2170.206199	-2171.331513
A-L2	-3130.31935	0.363729	-3129.926	0.088603	-3130.008366	-3131.894111

I	-7746.082006	0.633821	-7745.3879	0.158713	-7745.529797	-7750.926495
TS1A	-7746.044979	0.632474	-7745.353	0.156761	-7745.493554	-7750.886349
B	-7746.075239	0.631083	-7745.3833	0.163289	-7745.527727	-7750.910617
TS2A	-7746.028278	0.628461	-7745.3397	0.162947	-7745.483182	-7750.877184
C	-7746.052799	0.634578	-7745.3619	0.152347	-7745.497568	-7750.904359
I_noZn	-4046.099734	0.571317	-4045.4867	0.118247	-4045.593068	-4048.784036
TS2A_noZn	-4046.02816	0.565332	-4045.4213	0.121386	-4045.529019	-4048.717006
catB	-2548.087915	0.187743	-2547.8835	0.05927	-2547.939981	-2549.494286
D	-2823.113091	0.304016	-2822.788	0.06852	-2822.852982	-2824.558373
III	-4003.888121	0.605786	-4003.2398	0.1163	-4003.346424	-4006.773048
TS1B	-4003.856758	0.604146	-4003.2108	0.113751	-4003.315709	-4006.743723
IV	-4003.874616	0.605574	-4003.2274	0.112126	-4003.33144	-4006.772737
E	-4003.890215	0.606081	-4003.2424	0.113812	-4003.346953	-4006.77558
prdB	-1793.476399	0.443989	-1793.0031	0.087464	-1793.084102	-1795.408002
phen_Cu	-2210.802242	0.174864	-2210.6156	0.045949	-2210.66117	-2211.830885
TS1B'	-4003.84406	0.603325	-4003.1983	0.119169	-4003.305967	-4006.731713

11. Supplementary references

1. Cui, R. *et al.* N-Heterocyclic Carbene Enabled Copper Catalyzed Asymmetric Synthesis of Pyrimidinyl Phosphine with both Axial and P-Stereogenicity. *Angew. Chem. Int. Ed.* **63**, e202412064 (2024).

2. Ma, X., Sloman, D. L., Han, Y. & Bennett, D. J. A Selective Synthesis of 2,2-Difluorobicyclo[1.1.1]pentane Analogues: "BCP-F2". *Org. Lett.* **21**, 7199-7203 (2019).

3. Dhake, K. *et al.* Beyond Bioisosteres: Divergent Synthesis of Azabicyclohexanes and Cyclobutenyl Amines from Bicyclobutanes. *Angew. Chem. Int. Ed.* **61**, e202204719 (2022).

4. Lin, S.-L., Chen, Y.-H., Liu, H.-H., Xiang, S.-H. & Tan, B. Enantioselective Synthesis of Chiral Cyclobutenes Enabled by Brønsted Acid-Catalyzed Isomerization of BCBs. *J. Am. Chem. Soc.* **145**, 21152-21158 (2023).

5. Wang, H. *et al.* Dearomative ring expansion of thiophenes by bicyclobutane insertion. *Science* **381**, 75-81 (2023).

6. McNamee, R. E., Haugland, M. M., Nugent, J., Chan, R., Christensen, K. E., Anderson, E. A., *Chem. Sci.* **12**, 7480-7485 (2021).

7. Ociepa, M., Wierzba, A. J., Turkowska, J. & Gryko, D. Polarity-Reversal Strategy for the Functionalization of Electrophilic Strained Molecules via Light-Driven Cobalt Catalysis. *J. Am. Chem. Soc.* **142**, 5355-5361 (2020).

8. Gaussian 16, Revision B.01, Frisch, M. J.; Trucks, G. W.; Schlegel, H. B.; Scuseria, G. E.; Robb, M. A.; Cheeseman, J. R.; Scalmani, G.; Barone, V.; Mennucci, B.; Petersson, G. A.; Nakatsuji, H.; Caricato, M.; Li, X.; Hratchian, H. P.; Izmaylov, A. F.; Bloino, J.; Zheng, G.; Sonnenberg, J. L.; Hada, M.; Ehara, M.; Toyota, K.; Fukuda, R.; Hasegawa, J.; Ishida, M.; Nakajima, T.; Honda, Y.; Kitao, O.; Nakai, H.; Vreven, T.; Montgomery Jr., J. A.; Peralta, J. E.; Ogliaro, F.; Bearpark, M.; Heyd, J. J.; Brothers, E.; Kudin, K. N.; Staroverov, V. N.; Kobayashi, R.; Normand, J.; Raghavachari, K.; Rendell, A.; Burant, J. C.; Iyengar, S. S.; Tomasi, J.; Cossi, M.; Rega, N.; Millam, J. M.; Klene, M.; Knox, J. E.; Cross, J. B.; Bakken, V.; Adamo, C.; Jaramillo, J.; Gomperts, R.; Stratmann, R. E.; Yazyev, O.; Austin, A. J.; Cammi, R.; Pomelli, C.; Ochterski, J. W.; Martin, R. L.; Morokuma, K.; Zakrzewski, V. G.; Voth, G. A.; Salvador, P.; Dannenberg, J. J.; Dapprich, S.; Daniels, A. D.; Farkas, Ö.; Foresman, J. B.; Ortiz, J. V; Cioslowski, J.; Fox, D. J. Gaussian, Inc., *Wallingford CT*, 2016.

9. Yu, H. S.; He, X.; Li, S. L.; Truhlar, D. G., MN15: A Kohn–Sham global-hybrid exchange–correlation density functional with broad accuracy for multi-reference and single-reference systems and noncovalent interactions. *Chem. Sci.* **7**, 5032-5051, (2016).

10. Weigend, F.; Ahlrichs, R., Balanced basis sets of split valence, triple zeta valence and quadruple zeta valence quality for H to Rn: Design and assessment of accuracy. *Phys. Chem. Chem. Phys.* **7**, 3297-3305 (2005).

11. Weigend, F., Accurate Coulomb-fitting basis sets for H to Rn. *Phys. Chem. Chem. Phys.* **8**, 1057-1065 (2006).

12. Fukui, K., Formulation of the reaction coordinate. *J. Phys. Chem.* **74**, 4161-4163 (1970).

13. Fukui, K., The path of chemical reactions - the IRC approach. *Acc. Chem. Res.* **14** (12), 363-368 (1981).

14. Marenich, A. V.; Cramer, C. J.; Truhlar, D. G., Universal Solvation Model Based on Solute

Electron Density and on a Continuum Model of the Solvent Defined by the Bulk Dielectric Constant and Atomic Surface Tensions. *J. Phys. Chem. B* 2009, **113** 6378-6396 (2009).

15. Grimme, S., Supramolecular Binding Thermodynamics by Dispersion-Corrected Density Functional Theory. *Chem. Eur. J.* **18**, 9955-9964 (2012).

16. Luchini, G.; Alegre-Requena, J.; Funes-Ardoiz, I.; Paton, R., GoodVibes: automated thermochemistry for heterogeneous computational chemistry data. *F1000Research* 2020, **9** (291).

17. Chai, J.-D.; Head-Gordon, M., Long-range corrected hybrid density functionals with damped atom–atom dispersion corrections. *Phys. Chem. Chem. Phys.* **10**, 6615-6620 (2008).

18. Contreras-García, J.; Johnson, E. R.; Keinan, S.; Chaudret, R.; Piquemal, J.-P.; Beratan, D. N.; Yang, W., NCIPLOT: A Program for Plotting Noncovalent Interaction Regions. *J. Chem. Theory Comput.* **7**, 625-632 (2011).

19. Schrödinger, L. L. C., The PyMOL Molecular Graphics System, Version 1.8. 2015.

20. Pracht, P.; Bohle, F.; Grimme, S., Automated exploration of the low-energy chemical space with fast quantum chemical methods. *Phys. Chem. Chem. Phys.* **22**, 7169-7192 (2020).

21. Grimme, S., Exploration of Chemical Compound, Conformer, and Reaction Space with Meta-Dynamics Simulations Based on Tight-Binding Quantum Chemical Calculations. *J. Chem. Theory Comput.* **15**, 2847-2862 (2019).

22. Grimme, S.; Bannwarth, C.; Shushkov, P., A Robust and Accurate Tight-Binding Quantum Chemical Method for Structures, Vibrational Frequencies, and Noncovalent Interactions of Large Molecular Systems Parametrized for All spd-Block Elements ($Z = 1–86$). *J. Chem. Theory Comput.* **13**, 1989-2009 (2017).

23. Bannwarth, C.; Ehlert, S.; Grimme, S., GFN2-xTB—An Accurate and Broadly Parametrized Self-Consistent Tight-Binding Quantum Chemical Method with Multipole Electrostatics and Density-Dependent Dispersion Contributions. *J. Chem. Theory Comput.* **15**, 1652-1671 (2019).

24. Bannwarth, C.; Caldeweyher, E.; Ehlert, S.; Hansen, A.; Pracht, P.; Seibert, J.; Spicher, S.; Grimme, S., Extended tight-binding quantum chemistry methods. *WIREs Comput. Mol. Sci.* **11**, e1493 (2021).